

1 Title

2 **Deep-learning-based cell composition analysis from tissue expression profiles.**

3 Kevin Menden[§], Mohamed Marouf, Anupriya Dalmia, Peter Heutink, Stefan Bonn[§]

4

5 [§] Correspondence to sbonn@uke.de & Kevin.Menden@dzne.de

6 Abstract

7 We present Scaden, a deep neural network for cell deconvolution that uses gene
8 expression information to infer the cellular composition of tissues. Scaden is trained
9 on single cell RNA-seq data to engineer discriminative features that confer robustness
10 to bias and noise, making complex data preprocessing and feature selection
11 unnecessary. We demonstrate that Scaden outperforms existing deconvolution
12 algorithms in both precision and robustness, across tissues and species. A single
13 trained network reliably deconvolves bulk RNA-seq and microarray, human and
14 mouse tissue expression data. Due to this stability and flexibility, we surmise that deep
15 learning-based cell deconvolution will become a mainstay across data types and
16 algorithmic approaches. Scaden's comprehensive software package is easy to use on
17 novel as well as diverse existing expression datasets available in public resources,
18 deepening the molecular and cellular understanding of developmental and disease
19 processes.

20 Keywords

21 Cell Deconvolution, Deep Learning, Machine Learning, single cell RNA sequencing,
22 RNA sequencing, Deep Sequencing, Source Separation.

23 Introduction

24 The analysis of tissue-specific gene expression using Next Generation Sequencing
25 (RNA-seq) is a centerpiece of the molecular characterization of biological and medical
26 processes¹. A well-known limitation of tissue-based RNA-seq is that it typically
27 measures average gene expression across many molecularly diverse cell types that
28 can have distinct cellular states². A change in gene expression between two conditions
29 can therefore be attributed to a change in the cellular composition of the tissue or a
30 change in gene expression in a specific cell population, or a mixture of the two. To
31 deconvolve systematic differences in cell type composition is especially important in
32 systems with cellular proliferation (e.g. cancer) or cellular death (e.g. neuronal loss in
33 Neurodegenerative Diseases)³.

34 To account for this problem, several computational cell deconvolution methods have
35 been proposed during the last years^{4,5}. These algorithms attempt to calculate an
36 approximation of the cell type composition of a given gene expression sample, such
37 that systematic differences in cellular abundance between samples can be detected,
38 interpreted, and possibly corrected for. Current algorithms utilize gene expression
39 profiles (GEPs) of cell type-specifically expressed genes to estimate cellular fractions
40 using linear regression⁴. While the best performing linear regression algorithms for
41 deconvolution seem to be variations of Support Vector Regression (SVR)⁶⁻¹⁰, the
42 selection of an optimal GEP is a field of active research^{10,11}. Indeed, it has been
43 recently shown that the design of the GEP is the most important factor in most
44 deconvolution methods, as results from different algorithms strongly correlate given
45 the same GEP¹¹.

46 In theory, an optimal GEP should contain a set of genes that are predominantly
47 expressed within each cell population of a complex sample¹². They should be stably

48 expressed across experimental conditions, for example across health and disease,
49 and resilient to experimental noise and bias. The negative impact of bias on
50 deconvolution performance can be partly improved by using large, heterogeneous
51 GEP matrices¹¹. It is therefore not surprising that recent advancement in cell
52 deconvolution relied almost exclusively on sophisticated algorithms to normalize the
53 data and engineer optimal GEPs¹⁰.

54 While GEP-based approaches lay the foundational basis of modern cell deconvolution
55 algorithms, we hypothesize that Deep Neural Networks (DNNs) could create optimal
56 features for cell deconvolution, without relying on the complex generation of GEPs.
57 DNNs such as multilayer perceptrons are universal function approximators that
58 achieve state-of-the-art performance on classification and regression tasks. We
59 theorize that by using gene expression information as network input, hidden layer
60 nodes of the DNN would represent higher-order latent representations of cell types
61 that are robust to input noise and technical bias.

62 An obvious limitation of DNNs is the requirement for large training data to avoid
63 overfitting of the machine learning model. While ground truth information on tissue
64 RNA-seq cell composition is scarce, one can use single cell RNA-seq (scRNA-seq)
65 data to obtain virtually unlimited *in silico* tissue datasets of predefined cell
66 composition^{7-9,13-15}. This is achieved by sub-sampling and subsequently merging cells
67 from scRNA-seq datasets and is limited only by the availability of tissue-specific
68 scRNA-seq data. It is to be noted that scRNA-seq data suffers from known biases,
69 such as drop-out, that RNA-seq data is not subject to¹⁶. While this complicates the use
70 of scRNA-seq data for GEP design⁸, we surmise that latent network nodes could
71 represent features that are robust to such biases.

72 Based on these assumptions we developed a single-cell-assisted deconvolutional
73 DNN (Scaden) that uses simulated bulk RNA-seq samples for training and predicts
74 cell type proportions for input expression samples of cell mixtures. Scaden is trained
75 on publicly available scRNA- and RNA-seq data, does not rely on specific GEP
76 matrices, and automatically infers informative features. Finally, we show that Scaden
77 deconvolves expression data into cell types with higher precision and robustness than
78 existing methods that rely on GEP matrices, across tissues, species, and data types.

79 Results

80 Scaden Overview, Model Selection, and Training

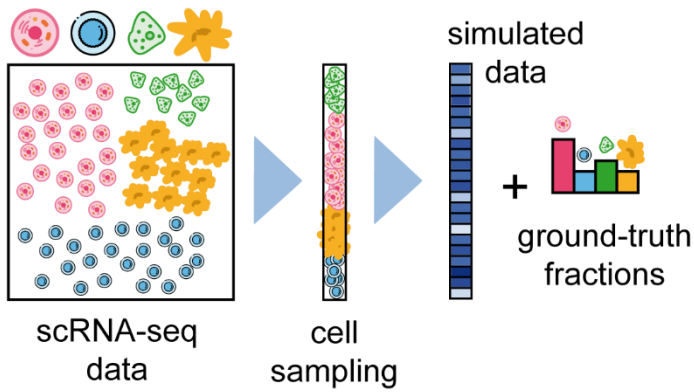
81 The basic architecture of Scaden is a DNN that takes gene counts of RNA-seq data
82 as input and outputs predicted cell fractions (Fig. 1). To optimize the performance of
83 the DNN, it is trained on data that contains both the gene expression and the real cell
84 fraction information (Fig. 1A). The network then adjusts its weights to minimize the
85 error between the predicted cell fractions and the real cell fractions (Fig. 1B).

86 For the model selection and training we made use of the virtually unlimited amount of
87 artificial bulk RNA-seq datasets with defined composition that can be generated *in*
88 *silico* from published scRNA-seq and RNA-seq datasets (simulated tissues) (Fig. 1,
89 Tables S1 & S2). The only constraint being that the scRNA-seq and RNA-seq data
90 must come from the same tissue as the bulk data subject to deconvolution.

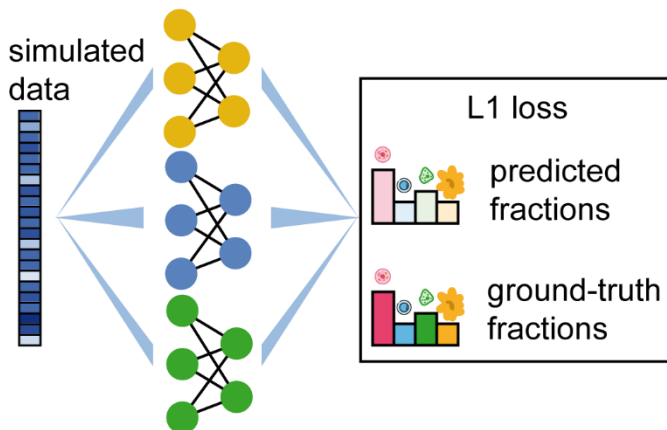
91 To find the optimal DNN architecture for cell deconvolution, we performed leave-one-
92 dataset-out cross validation on simulated peripheral blood mononuclear cell (PBMC)
93 tissue, training on mixtures of three scRNA-seq datasets and evaluating the
94 performance on simulated tissue from a fourth scRNA-seq dataset (Table S1 & S3).

95 The final Scaden model is an ensemble of the three best performing models and the
96 final cell type composition estimates are the averaged predictions of all three
97 ensemble models (Fig. S1, Table S4).
98

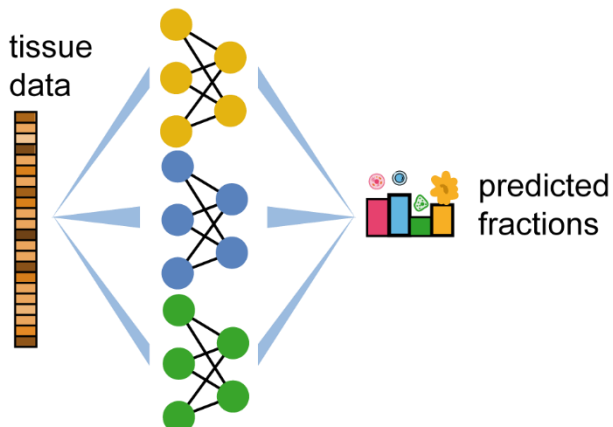
A Simulated training data



B Scaden training



C Scaden predictions



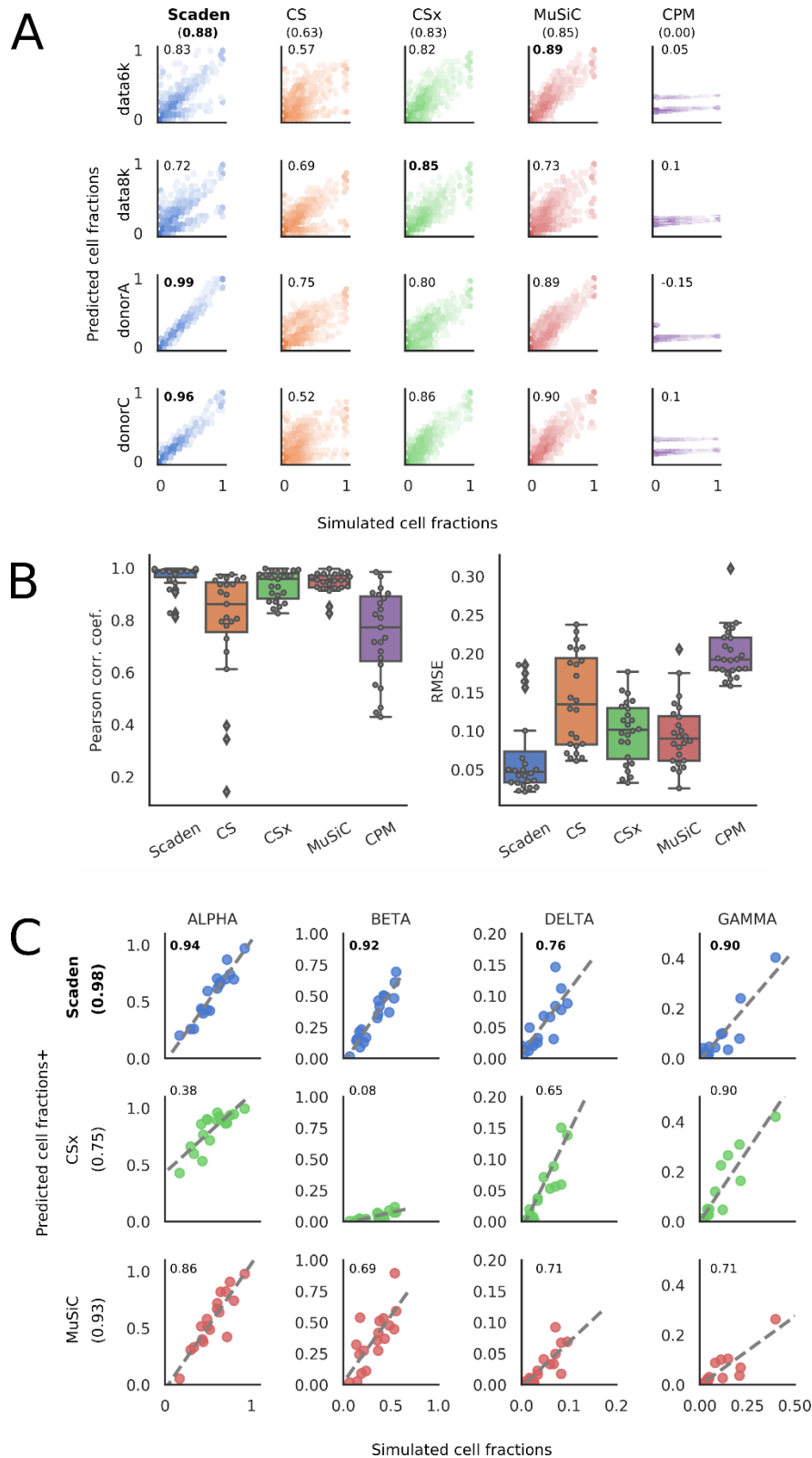
99

100 **Figure 1** Overview of training data generation and cell type deconvolution with Scaden. A:
101 Artificial bulk samples are generated by subsampling random cells from a scRNA-seq datasets
102 and merging their expression profiles. B: Model training and parameter optimization on
103 simulated tissue RNA-seq data by comparing cell fraction predictions to ground-truth cell
104 composition. C: Cell deconvolution of real tissue RNA-seq data using Scaden.

105

106 To get an initial estimate of Scaden's deconvolution fidelity we measured the root
107 mean square error (RMSE), Lin's concordance correlation coefficient (CCC)¹⁷,
108 Pearson's correlation coefficient (r), and the slope and intercept of the regression fitted
109 for actual and predicted cell fractions. To this end, 32,000 human PBMC, 14,000
110 human pancreas, 6,000 human ascites, and 30,000 mouse brain simulated tissue
111 samples were generated for network training and evaluation (Table S2). We then
112 compared Scaden to four state-of-the-art GEP-based cell deconvolution algorithms,
113 CIBERSORT (CS)⁶, CIBERSORTx (CSx)⁷, MuSiC⁸, and Cell Population Mapping
114 (CPM)⁹. While CS relies on hand-curated GEP matrices, CSx, MuSiC, and CPM can
115 generate GEPs using scRNA-seq data as input.

116 We first evaluated the deconvolution performance on simulated PBMC data, since
117 curated GEP matrices and RNA-seq datasets with associated ground truth cell type
118 compositions are available for human PBMCs, making this tissue uniquely suited
119 toward deconvolution performance evaluation. Scaden was trained on simulated data
120 from all datasets but a held-out dataset while CSx, MuSiC and CPM used a GEP
121 generated from a scRNA-seq dataset excluding a held-out dataset (e.g. data6k,
122 data8k, donorA). Subsequently the algorithms were tested on 500 simulated PBMC
123 samples from a held-out scRNA-seq dataset (e.g. donorC) (Fig. 2A & B, Table S5).
124 For CS we used the PBMC-optimized LM22 GEP matrix⁶ and tested performance on
125 the 500 simulated PBMC samples from a held-out scRNA-seq dataset (e.g. donorC).



126

127 **Figure 2** Deconvolution performance on simulated tissue data A: Ground truth values (x-axis)
 128 plotted against cell type fraction estimates (y-axis) for predictions made on simulated data
 129 from four PBMC scRNA-seq datasets. Darker color in a hexbin corresponds to more data
 130 points falling into this bin. Numbers inside the plotting area signify CCC values, the overall

131 CCC is shown in parenthesis below the algorithm name. B: Boxplots of r and RMSE values
132 for simulated PBMC data. C: Per-cell-type scatterplots of ground truth (x-axis) and predicted
133 values (y-axis) for Scaden, CSx, and MuSiC on artificial pancreas data¹⁸. Numbers inside the
134 plotting area signify CCC values.

135

136 For two of four test datasets (donorA, donorC), Scaden obtained the highest CCC and
137 lowest RMSE, followed by CSx, MuSiC, CS, and CPM (Fig. 2A, Table S5). CSx and
138 MuSiC obtain the highest CCC values for the data8k and data6k datasets,
139 respectively. Overall, Scaden obtains the highest CCC and lowest RMSE (0.88, 0.08,
140 respectively), followed by MuSiC(0.85, 0.10), CSx(0.83, 0.11), CS (0.63 0.15), and
141 CPM (0, 0.20) (Fig. 2A). As expected, all algorithms that use scRNA-seq data as
142 reference perform good in this scenario with the notable exception of CPM. We want
143 to mention that CPM was not primarily developed for cell deconvolution, but merely
144 incorporates this as an additional feature. On average, Scaden also obtained the
145 highest correlation and the best intercept and slope values on simulated PBMC data
146 (Table S5).

147 A specific feature of the MuSiC algorithm is that it preferentially weighs genes
148 according to low inter-subject and intra-cell cluster variability for its GEP, which
149 increases deconvolution robustness when high expression heterogeneity is observed
150 between human subjects, for example⁸. To understand if Scaden can utilize multi-
151 subject information to increase its deconvolution performance, we trained Scaden,
152 CSx, and MuSiC on scRNA-seq pancreas data from several subjects¹⁹ and assessed
153 the performance on a separate simulated pancreas RNA-seq dataset¹⁸ (Fig. 2C, Table
154 S6). To allow for direct comparison, we chose the same pancreas training and test
155 datasets that were used in the original MuSiC publication (Table S1). To enable
156 Scaden to leverage the heterogeneity of multi-subject data, training data was

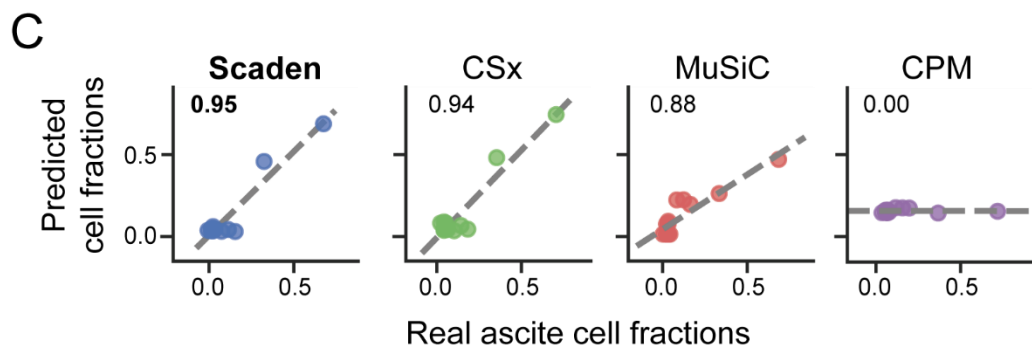
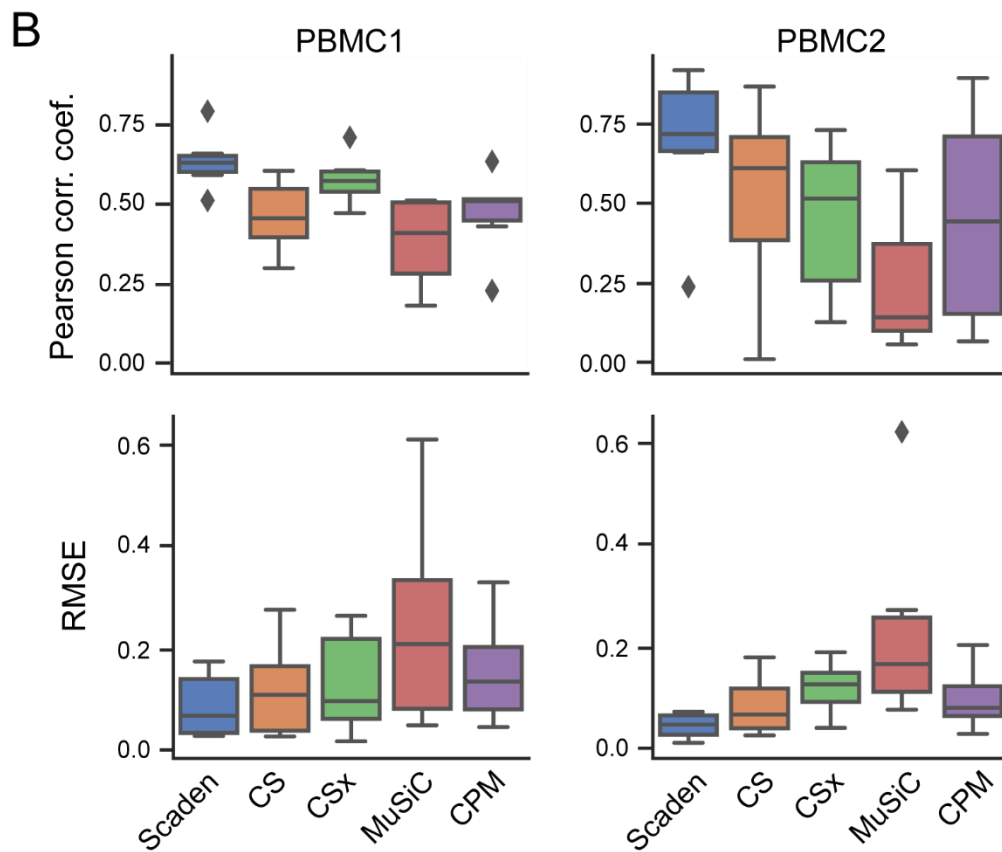
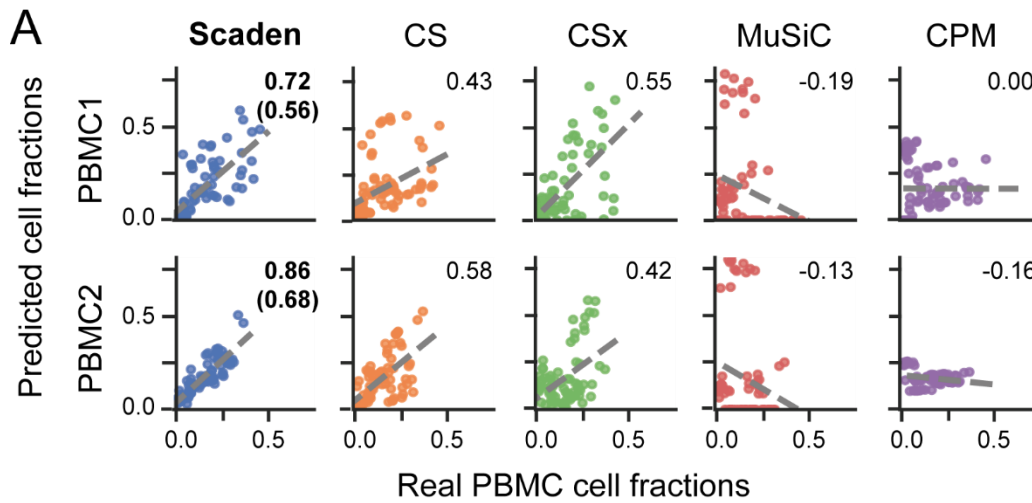
157 generated separately for every subject in the dataset (see Methods). CSx cannot profit
158 from multi-subject data but performed well on the artificial PBMC datasets and was
159 therefore included in the comparison. The best performance is achieved by Scaden
160 (CCC = 0.98), closely followed by MuSiC (CCC = 0.93), while CSx does not perform
161 as well (CCC = 0.75) (Fig. 2C, Table S6). This provides strong evidence that Scaden,
162 by separating training data generation for each subject, can learn inter-subject
163 heterogeneity and outperform specialized multi-subject algorithms such as MuSiC on
164 the cell-type deconvolution task.

165 Additionally, we wanted to test how the best performing deconvolution algorithms
166 Scaden, MuSiC, and CSx behave when unknown cell content is part of the mixture.
167 To test this, all cells falling into the 'Unknown' category were removed from the training
168 or reference datasets but added to the simulated mixture samples at fixed percentages
169 (5%, 10%, 20%, 30%) (see Methods). Scaden obtains the highest CCC for all tested
170 percentages of unknown cell content (Fig. S2, Table S8). The general deconvolution
171 performance declines linearly with increasing percentage of unknown content for all
172 tested algorithms (Fig. S2, Table S8), indicating that Scaden, MuSiC, and CSx have a
173 similar robustness against unknown mixture content.

174 Robust deconvolution of bulk expression data

175 The true use case of cell deconvolution algorithms is the cell fraction estimation of
176 tissue RNA-seq data. We therefore assessed the performance of Scaden, CS, CSx,
177 MuSiC, and CPM to deconvolve two publicly available human PBMC bulk RNA-seq
178 datasets, for which ground-truth cell composition information was measured using flow
179 cytometry (Fig. 3A, Tables S7 & S9). We will refer to these datasets that consists of
180 12 samples each as PBMC1²⁰ and PBMC2¹⁰. Deconvolution for all methods was

181 performed as described in the previous section, with the difference that data from all
182 four PBMC scRNA-seq datasets was now deployed for Scaden training.



183

184 **Figure 3** *Deconvolution of real tissue RNA-seq data* A: Per-cell-type scatterplots of ground
185 truth (x-axis) and predicted values (y-axis) for Scaden, CS, CSx, MuSiC, and CPM on real
186 PBMC1 and PBMC2 cell fractions. Numbers inside the plotting area signify CCC values. For
187 Scaden, the CCC using only scRNA-seq training data (in parenthesis) and the CCC using
188 mixed scRNA-seq and RNA-seq training data is shown. B: Boxplots of r (first row) and RMSE
189 (second row) values for real PBMC1 (first column) and PBMC2 (second column) data. C: Per-
190 cell-type scatterplots of ground truth (x-axis) and predicted values (y-axis) for Scaden, CSx,
191 MuSiC, and CPM on real ascite cell fractions. Numbers inside the plotting area signify CCC
192 values.

193
194 On the PBMC1 dataset, Scaden obtained the highest CCC and lowest RMSE (0.56,
195 0.13), while CSx (0.55, 0.16) and CS (0.43, 0.15) performed well yet significantly worse
196 than Scaden (Fig. 3A, Tables S8 & S9). CPM (0, 0.18) and MuSiC (-0.19, 0.32) both
197 failed to deconvolve the cell fractions of the PBMC1 data. Scaden also obtained the
198 best CCC and RMSE (0.68, 0.08) on the PBMC2 dataset, while CS (0.58, 0.10) and
199 CSx (0.42, 0.13) obtained good deconvolution results. Similar to the PBMC1 data
200 deconvolution results, CPM (-0.16, 0.11) as well as MuSiC (-0.13, 0.30) did not
201 perform well on the PBMC2 deconvolution task. In addition to CCC and RMSE metrics,
202 Scaden achieves the best correlation, intercept and slope on both PBMC datasets
203 (Tables S9 & S10).

204 An additional algorithmic feature of Scaden is that it seamlessly integrates increasing
205 amounts of training data, which can be of different types, such as a combination of
206 simulated tissue and real tissue data with cell fraction information. In theory, even
207 limited real tissue training data could make Scaden robust to data type bias and
208 consequently improve Scaden's deconvolution performance on real tissue data. We
209 therefore trained Scaden on a mix of simulated PBMC (500 samples) and real PBMC2
210 (12 samples) data and evaluated its performance on real PBMC1 data (Fig. 3A, S3,

211 Table S9). While the training contained only ~2% real data, Scaden's CCC increased
212 from 0.56 to 0.72 and the RMSE decreased from 0.13 to 0.10. We observed similar
213 performance increases when Scaden was trained on simulated PBMC and real
214 PBMC1 data and evaluated on real PBMC2 data (Fig. 3A, S3, Table S10).

215 We next evaluated Scaden's performance on real ascites RNA-seq data, for which
216 scRNA-seq and FACS cell proportion data is available²¹ (Table S7). It is noteworthy
217 that RNA-seq, scRNA-seq, and FACS data was generated for the same samples,
218 which potentially entails reduced experimental and technical bias and consequently
219 higher deconvolution fidelity for the ascites data as compared to the PBMC data. We
220 did not evaluate CS's performance on the ascites data as there was no optimized
221 ascites GEP available. For Scaden, CSx, CPM and MuSiC we used scRNA-seq data
222 to generate either simulated tissue data for training (Scaden) or a reference GEP (CSx,
223 CPM, MuSiC). Scaden, CSx, CPM, and MuSiC all accurately predict the cell type
224 compositions for the three real ascites samples, while CPM does not perform well (Fig.
225 3C, Table S11). The highest CCC and lowest RMSE were achieved by Scaden (0.95,
226 0.06), followed by CSx (0.94, 0.07), MuSiC (0.88, 0.08), and CPM (0, 0.18). This
227 further validates that Scaden reliably deconvolves tissue RNA-seq data into the
228 constituent cell fractions and that very accurate deconvolution results can be obtained
229 if reference and target datasets are from the same experiment. Again, we stress that
230 CPM was not primarily developed for cell deconvolution, but mainly for a different
231 functionality.

232 We next wanted to assess if Scaden's deconvolution performance is robust across
233 species. We therefore tested whether a Scaden model trained on mouse brain scRNA-
234 seq data could generate reasonable cell composition estimations for real human brain
235 RNA-seq data (Table S7). To this end, Scaden was trained on artificial data generated

236 from five mouse brain scRNA-seq datasets and predicted the cell fractions on human
237 post-mortem RNA-seq brain samples (390 prefrontal cortex samples) from the
238 ROSMAP study²². Ground-truth cell fractions were not available for this data, which is
239 why we used Braak stages²³ that correspond to Alzheimer's disease severity and
240 correlate with the degree of neuronal loss. Overall, Scaden's cell fraction predictions
241 capture the increased neuronal loss with increasing Braak stage (Fig. S4).
242 Interestingly, the largest drop in neural percentage is observed at stage 5, when the
243 neurodegeneration typically reaches the prefrontal cortex of the brain. By learning
244 robust features, Scaden reliably deconvolves RNA-seq data in a cross-species
245 comparison.

246 Given the robustness with which Scaden predicts tissue RNA-seq cell fractions using
247 scRNA-seq training data, even across species, we next wanted to investigate if a
248 scRNA-seq-trained Scaden model can also deconvolve other data types. To this end,
249 we measured the deconvolution performance on a bulk PBMC microarray dataset (20
250 samples)⁶ of a Scaden model trained on scRNA-seq and RNA-seq PBMC data (see
251 above). We compared Scaden to CS using the microarray-derived LM22 matrix. CS
252 achieved a slightly higher CCC and slightly lower total RMSE (0.72, 0.11) than Scaden
253 (0.71, 0.13), while Scaden obtained the highest average CCC (0.50) compared to CS
254 (0.39) (Fig. S5, Table S12). Notably in this scenario, Scaden was trained entirely on
255 simulated data and RNA-seq data, while CS's LM22 GEP was optimized on PBMC
256 microarray data.

257 Overall, we provide strong evidence that Scaden robustly deconvolves tissue data
258 across tissues, species, and even data types.

259 Discussion

260 Scaden is the first deep learning-based cell deconvolution algorithm. In many
261 instances, it compares favorably in both prediction robustness and accuracy to existing
262 deconvolution algorithms that rely on GEP design and linear regression. We believe
263 that Scaden's performance relies to a large degree on the inherent feature engineering
264 of the DNN. The network does not only select features (genes) for regression, it also
265 creates novel features that are optimal for the regression task in the nodes of the
266 hidden layers. These hidden features are non-linear combinations of the input features
267 (gene expression), which makes it notoriously difficult to explain how a DNN works²⁴.
268 It is important to highlight that this feature creation is fundamentally different from all
269 other existing cell deconvolution algorithms, which rely on heuristics that select a
270 defined subset of genes as features for linear regression.

271 Another advantage of this inherent feature engineering is that Scaden can be trained
272 to be robust to input noise and bias (e.g. batch effects). Noise and bias are all prevalent
273 in experimental data, due to different sample quality, sample processing,
274 experimenters, and instrumentation, for example. If the network is trained on different
275 datasets of the same tissue, however, it learns to create hidden features that are
276 robust to noise and bias, such as batch effects. This robustness is pivotal in real world
277 cell deconvolution use cases, where the bulk RNA data for deconvolution and the
278 training data (and therefore the network and GEP) contain different noise and biases.
279 While especially recent cell deconvolution algorithms include batch correction
280 heuristics prior to GEP construction, Scaden optimizes its hidden features
281 automatically when trained on data from various batches.

282 The robustness to noise and bias, which might be due to hidden feature generation, is
283 especially evident in Scaden's ability to deconvolve across data types. A network

284 trained on *in silico* bulk RNA-seq data can seamlessly deconvolve microarray data of
285 the same tissue. This is quite noteworthy, as microarray data is known to have a
286 reduced dynamic range and several hybridization-based biases compared to RNA-
287 seq data. In other words, Scaden can deconvolve bulk data of types it has never been
288 trained on, even in the face of strong data type bias. This raises the possibility that
289 Scaden trained on scRNA-seq data might reliably deconvolve other bulk omics data
290 as well, such as proteomic and metabolomic data. This assumption is strengthened
291 by the fact that Scaden, trained on scRNA-seq data, attains state-of-the-art
292 performance on the deconvolution of bulk RNA-seq data, two data types with very
293 distinct biases¹⁶.

294 As highlighted in the introduction, a drawback for many DNNs is the large amount of
295 training data required to obtain robust performance. Here, we used scRNA-seq data
296 to create virtually unlimited amounts of *in silico* bulk RNA-seq data of predefined type
297 (target tissue) with known composition, across datasets. This immediately highlights
298 Scaden's biggest limitation, the dependency on scRNA-seq data of the target tissue.
299 In this study we have shown that Scaden, trained solely on simulated data from
300 scRNA-seq datasets, can outperform GEP-based deconvolution algorithms. We did
301 observe, however, that the addition of labeled RNA-seq samples to the training data
302 did significantly improve deconvolution performance in the case of PBMC data. We
303 therefore believe that efforts to increase the similarity between simulated training data
304 and the target bulk RNA-seq data could increase Scaden's performance further.
305 Mixtures of *in silico* bulk RNA-seq data and publically available RNA-seq data, of
306 purified cell types for example, could further increase the deconvolution performance
307 of Scaden. Furthermore, domain adaptation methods can be used to improve
308 performance of models that are trained on data (here, scRNA-seq data) that is similar

309 to the target data (here, RNA-seq data)²⁵. In future versions, Scaden's simple
310 multilayer perceptron architecture could leverage domain adaptation to further
311 stabilize and improve its cell deconvolution performance.

312 Recent cell deconvolution algorithms have used cell fraction estimates to infer cell
313 type-specific gene expression from bulk RNA-seq data. It is straightforward to use
314 Scaden's cell fraction estimates to infer per group³ and per sample⁷ cell type-specific
315 gene expression using simple regression or non-negative matrix factorization,
316 respectively. We would like to add a note of caution, however, as the error of cell
317 fraction estimates, which can be quite significant, is propagated into the gene
318 expression calculations and will affect any downstream statistical analysis.

319 In summary, the deconvolution performance, robustness to noise and bias, the
320 flexibility to learn from large numbers of *in silico* datasets, across data types (scRNA-
321 seq and RNA-seq mixtures), and potentially even tissues makes us believe that DNN-
322 based architectures will become an algorithmic mainstay of cell type deconvolution.

323

324 Methods

325 Datasets and pre-processing

326 scRNA-seq datasets

327 The following human PBMC scRNA-seq datasets were downloaded from the 10X
328 Genomics data download page: 6k PBMCs from a Healthy Donor, 8k PBMCs from a
329 Healthy Donor, Frozen PBMCs (Donor A), Frozen PBMCs (Donor C){Zheng et al,
330 2017}. Throughout this paper, these datasets are referred to with the handles data6k,
331 data8k, donorA and donorC, respectively. These four datasets were chosen because
332 of clearly identifiable cell types for the majority of cells. The Ascites scRNA-seq dataset
333 was downloaded from <https://figshare.com> as provided by Schelker²¹. Pancreas and
334 mouse brain datasets were downloaded from the scRNA-seq dataset collection of the
335 Hemberg lab (<https://hemberg-lab.github.io/scRNA.seq.datasets/>). A table listing all
336 datasets including references to the original publications can be found in Table S1.

337 scRNA-seq preprocessing and analysis

338 All datasets were processed using the Python package Scanpy (v. 1.2.2)²⁶ following
339 the Scanpy's reimplementation of the popular Seurat's clustering workflow. First, the
340 corresponding cell-gene matrices were filtered for cells with less than 500 detected
341 genes, and genes expressed in less than 5 cells. The resulting count matrix for each
342 dataset was filtered for outliers with high or low numbers of counts. Gene expression
343 was normalized to library size using the Scanpy function 'normalize_per_cell'. The
344 normalized matrix of all filtered cells and genes was saved for the subsequent data
345 generation step.

346 The following processing and analysis steps had the sole purpose of assigning cell
347 type labels to every cell. All cells were clustered using the louvain clustering
348 implementation of the Scanpy package. The louvain clustering resolution was chosen
349 for each dataset, using the lowest possible resolution value (low resolution values lead
350 to less clusters) for which the calculated clusters separated the cell types
351 appropriately. The top 1000 highly variable genes were used for clustering, which were
352 calculated using Scanpy's 'filter_genes_dispersion' function with parameters
353 min_mean=0.0125, max_mean=3 and min_disp=0.5. Principal Component Analysis
354 (PCA) was used for dimensionality reduction.

355 To identify cell types, marker genes were investigated for all cell types in question. For
356 PBMC datasets, useful marker genes were adopted from public resources such as the
357 Seurat tutorial for 2700 PBMCs²⁷. Briefly, IL7R was taken as marker for CD4 T-cells,
358 LYZ for Monocytes, MS4A1 for B-cells, GNLY for Natural Killer cells, FCER1A for
359 Dendritic cells and CD8A and CCL5 as markers for CD8 T-cells. For all other scRNA-
360 seq datasets, marker genes and expected cell types were inferred from the original
361 publication of the dataset. For instance, to annotate cell types of the mouse brain
362 dataset from Zeisel et al.²⁸, we used the same marker genes as Zeisel and colleagues.
363 We did not use the same cell type labels from the original publications because a main
364 objective was to assure that cell type labeling is consistent between all datasets of a
365 certain tissue.

366 Cell type annotation was performed manually across all the clusters for each dataset,
367 such that all cells belonging to the same cluster were labeled with the same cell type.
368 The cell type identity of each cluster was chosen by crossing the cluster's highly
369 differentially expressed genes with the curated cell type's marker genes. Clusters that

370 could not be clearly identified with a cell type were grouped into the ‘Unknown’
371 category.

372 Tissue Datasets for Benchmarking

373 To assess the deconvolution performance on real tissue expression data, we used
374 datasets for which the corresponding cell fractions were measured and published. The
375 first dataset is the **PBMC1** dataset which was obtained from Zimmermann *et al.*²⁰. The
376 second dataset, **PBMC2**, was downloaded from GEO with accession code
377 GSE107011¹⁰. This dataset contains both RNA-seq profiles of immune cells (S4
378 cohort) and from bulk individuals (S13 cohort). As we were interested in the bulk
379 profiles, we only used 12 samples from the S13 cohort from this data. Flow cytometry
380 fractions were collected from the Monaco *et al.* publication¹⁰.

381 In addition to the above mentioned two PBMC datasets, we used Ascites RNA-seq
382 data. This dataset was kindly provided by the authors and cell type fractions for this
383 dataset were taken from the supplementary materials of the publication²¹.

384 For the evaluation on pancreas data, artificial bulk RNA-seq samples created from the
385 scRNA-seq dataset of Xin *et al.*¹⁸ were used. This dataset was downloaded from the
386 resources of the MuSiC publication⁸. The artificial bulk RNA-seq samples used for
387 evaluation were then created using the ‘bulk_construct’ function of the MuSiC tool.

388 To assess how Scaden deals with unknown cell types in a bulk mixture, we used the
389 whole blood dataset from Newman *et al.*⁷, which consists of 12 samples (GSE127813).

390 Cell type fractions were downloaded from the CSx website
391 (<https://cibersortx.stanford.edu/download.php>).

392 To assess robustness against unknown mixture content, all cells classified as
393 ‘Unknown’ were removed from the data6k, data8k, donorA, and donorC datasets to
394 generate training samples for Scaden and reference datasets for MuSiC and CSx.

395 Then, test datasets were generated with fixed content of 'Unknown' cells at 5%, 10%,
396 20% and 30%. Performance on these samples was then assessed to test robustness
397 against unseen cell types in the bulk mixture. Scaden was trained on samples from all
398 datasets but the test dataset, while CSx and MuSiC used data8k as a reference.

399 The microarray dataset GSE65133 was downloaded from GEO, and cell type fractions
400 taken from the original CS publication⁶.

401 Finally, we wanted to get insights into neurodegenerative cell fraction changes in the
402 brain. While it is known that neurodegenerative diseases like Alzheimer's Disease are
403 accompanied by a gradual loss of brain neurons, stage-specific cell type shifts are still
404 hard to come by. Here we use the ROSMAP (Religious Orders Study and Memory and
405 Aging Project Study) cortical RNA-seq dataset along with the corresponding clinical
406 metadata, to infer cell type composition over six clinically relevant stages of
407 neurodegeneration²².

408 RNA-seq preprocessing and analysis

409 For the RNA-seq datasets analyzed in this study, we did not apply any additional
410 processing steps, but used the obtained count or expression tables directly as
411 downloaded for all dataset except the ROSMAP dataset. For the latter, we generated
412 count tables from raw FastQ-files using Salmon²⁹ and the GRCh38 reference genome.
413 FastQ-files from the ROSMAP study were downloaded from Synapse
414 (www.synapse.org).

415 Simulation of bulk RNA-seq samples from scRNA-seq data

416 Scaden's deep neural network requires large amounts of training RNA-seq samples
417 with known cell fractions. This explains why the generation of artificial bulk RNA-seq
418 data is one of the key elements of the Scaden workflow.

419 In order to generate the training data, preprocessed scRNA-seq datasets were used
420 (see section ‘Data Collection and Processing’), comprising the gene expression matrix
421 and the cell type labels. Artificial RNA-seq samples were simulated by sub-sampling
422 cells from individual scRNA-seq datasets - cells from different datasets were not
423 merged into samples to preserve within-subject relationships. Datasets generated
424 from multiple subjects were split according to subject and each sub-sampling was
425 constrained to cells from one subject in order to capture the cross-subject
426 heterogeneity and keep subject-specific gene dependencies.

427 The exact sub-sampling procedure is described in the following. First, for every
428 simulated sample, random fractions were created for all different cell types within each
429 scRNA-seq dataset using the random module of the Python package NumPy. Briefly,
430 a random number was chosen from a uniform distribution between 0 and 1 using the
431 NumPy function ‘random.rand()’ for each cell type, and then this number was divided
432 by the sum of all random numbers created to ensure the constraint of all fractions
433 adding up to 1:

$$434 \quad f_c = \frac{r_c}{\sum_{C_{all}} r_c}$$

435 where r_c is the random number created for cell type c , and C_{all} is the set of all cell
436 types. Here, f_c is the calculated random fraction for cell type c . Then, each fraction
437 was multiplied with the total number of cells selected for each sample, yielding the
438 number of cells to choose for a specific cell type:

$$439 \quad N_c = f_c * N_{total}$$

440
441
442 where N_c is the number of cells to select for the cell type c , and N_{total} is the total
443 number of cells contributing to one simulated RNA-seq sample (400, in this study).
444 Next, N_c cells were randomly sampled from the scRNA-seq gene expression matrix

445 for each cell type c . Afterwards, the randomly selected single-cell expression profiles
446 for every cell type are then aggregated by summing their expression values, to yield
447 the artificial bulk expression profile for this sample.

448 Using the above described approach, cell compositions that are strongly biased
449 toward a certain cell type or are missing specific cell types are rare among the
450 generated training samples. To account for this and to simulate cell compositions with
451 a heavy bias to and the absence of certain cell types, a variation of the sub-sampling
452 procedure was used to generate samples with sparse compositions, which we refer to
453 as sparse samples. Before generating the random fractions for all cell types, a random
454 number of cell types was selected to be absent from the sample, with the requirement
455 of at least one cell type constituting the sample. After these leave-out cell types were
456 chosen, random fractions were created and samples generated as described above.

457 Using this procedure, we generated 32,000 samples for the human PBMC training
458 dataset, 14,000 samples for the human pancreas training dataset and 30,000 samples
459 for the mouse brain training dataset (Table S2).

460 Artificial bulk RNA-seq datasets were stored in 'h5ad' format using the Anndata
461 package²⁶, which allows to store the samples together with their corresponding cell
462 type ratios, while also keeping information about the scRNA-seq dataset of origin for
463 each sample. This allowed to access samples from specific datasets, which is useful
464 for cross validation.

465 Scaden Overview

466 The following section contains an overview of the input data preprocessing, the
467 Scaden model, model selection, and how Scaden predictions are generated.

468 Input Data Preprocessing

469 The data preprocessing step is aimed to make the input data more suitable for
470 machine learning algorithms. To achieve this, an optimal preprocessing procedure
471 should transform any input data from the simulated samples or from the bulk RNA-seq
472 to the same feature scale. Before any scaling procedure can be applied, it must be
473 ensured that both the training data and the bulk RNA-seq data subject to prediction
474 share the same features. Therefore, before scaling, both datasets are limited to
475 contain features (genes) that are available in both datasets.. The two-step processing
476 procedure used for Scaden is described in the following:

477 First, to account for heteroscedasticity, a feature inherent to RNA-seq data, the data
478 was transformed into logarithmic space by adding a pseudocount of 1 and then taking
479 the Logarithm (base 2). Additional to stabilizing the variance, this transformation yields
480 data that is approximately Gaussian.

481 Second, every sample was scaled to the range [0,1] using the `MinMaxScaler()` class
482 from the Sklearn preprocessing module. Per sample scaling, unlike per feature scaling
483 that is more common in machine learning, assures that inter-gene relative expression
484 patterns in every sample are preserved. This is important, as our hypothesis was that
485 a neural network could learn the deconvolution from these inter-gene expression
486 patterns.

$$487 \quad x_{scaled,i} = (x_i - \min(X_i)) / (\max(X_i) - \min(X_i))$$

488 where $x_{scaled,i}$ is the log2 expression value of gene x in sample i, X_i is the vector of
489 log2 expression values for all genes of sample i, $\min(X_i)$ is the minimum gene
490 expression of vector X_i , and $\max(X_i)$ the maximum gene expression of vector X_i .

491 Note that all training datasets are stored as expression values and are only processed
492 as described above. In the deployment use-case the simulated training data should
493 contain the same features as in the bulk RNA-seq sample that shall be deconvolved.

494 Model Selection

495 The goal of model selection was to find an architecture and hyperparameters that
496 robustly deconvolve simulated tissue RNA-seq data and, more importantly, real bulk
497 RNA-seq data. Due to the very limited availability of bulk RNA-seq datasets with known
498 cell fractions, model selection was mainly optimized on the simulated PBMC datasets.
499 To capture inter-experimental variation, we used leave-one-dataset-out cross
500 validation for model optimization: a model was trained on simulated data from all but
501 one dataset, and performance was tested on simulated samples from the left-out
502 dataset. This allows to simulate batch effects between datasets and helps to test the
503 generalizability of the model. Model performance was evaluated based on pearson
504 product moment correlation and absolute deviation between predicted and ground
505 truth values. As averaging the predictions of models with different architectures
506 increased performance, we decided to use an ensemble architecture for Scaden. For
507 this ensemble, the three best performing architectures were chosen. Model training
508 and prediction is done separately for each model, with the prediction averaging step
509 combining all model predictions (Fig. S1). We provide a list of all tested parameters in
510 the supplementary materials (Table S4).

511 Final Scaden Model

512 The Scaden model learns cell type deconvolution through supervised training on
513 datasets of simulated bulk RNA-seq samples simulated with scRNA-seq data. To
514 account for model biases and to improve performance, Scaden consists of an

515 ensemble of three deep neural networks with varying architectures and degrees of
516 dropout regularization. All models of the ensemble use four layers of varying sizes
517 between 32 and 1024 nodes, with dropout-regularization implemented in two of the
518 three ensemble models. The exact layer sizes and dropout rates are listed in Table
519 S3. The Rectified Linear Unit (ReLU) is used as activation function in every internal
520 layer. We used a Softmax function to predict cell fractions, as we did not see any
521 improvements in using a linear output function with consecutive non-negativity
522 correction and sum-to-one scaling. Python (v. 3.6.6) and the TensorFlow library (v.
523 1.10.0) were used for implementation of Scaden. A complete list of all software used
524 for the implementation of Scaden is provided in Table S12.

525 Training and Prediction

526 After the preprocessing of the data a Scaden ensemble can be trained on simulated
527 tissue RNA-seq data or mixtures of simulated and real tissue RNA-seq data.
528 Parameters are optimized using Adam with a learning rate of 0.0001 and a batch size
529 of 128. We used an L1 loss as optimization objective:

$$530 \quad L1(y_i, \hat{y}_i) = |y_i - \hat{y}_i|$$

531 where y_i is the vector of ground truth fractions of sample i and \hat{y}_i is the vector of
532 predicted fractions of sample i . Each of the three ensemble models is trained
533 independently for 5,000 steps. This 'early stopping' serves to avoid domain overfitting
534 on the simulated tissue data, which would decrease the model performance on the
535 real tissue RNA-seq data. We observed that training for more steps lead to an average
536 performance decrease on real tissue RNA-seq data. To perform deconvolution with
537 Scaden, a bulk RNA-seq sample is fed into a trained Scaden ensemble and three
538 independent predictions for the cell type fractions of this sample are generated by the

539 trained deep neural networks. These three predictions are then averaged per cell type
540 to yield the final cell type composition for the input bulk RNA-seq sample:

$$541 \quad \hat{y}_c = \frac{\hat{y}_c^1 + \hat{y}_c^2 + \hat{y}_c^3}{3}$$

542 where \hat{y}_c is the final predicted fraction for cell type c and \hat{y}_c^i is the predicted fraction for
543 cell type c of model i .

544 Algorithm Comparison

545 We used several performance measures to compare Scaden to four existing cell
546 deconvolution algorithms, CIBERSORT with LM22 GEP (CS), CIBERSORTx (CSx),
547 MuSiC and CPM. To compare the performance of the five deconvolution algorithms
548 we measured the root mean squared error (RMSE), Lin's concordance correlation
549 coefficient CCC , Pearson product moment correlation coefficient r , and R^2 values
550 comparing real and predicted cell fractions estimates. Additionally, to identify
551 systematic prediction errors and biases, slope and intercept for the regression lines
552 were calculated. These metrics are defined as follows:

$$553 \quad RMSE(y, \hat{y}) = \sqrt{avg(y - \hat{y})^2}$$

$$554 \quad r(y, \hat{y}) = \frac{cov(y, \hat{y})}{\sigma_y \sigma_{\hat{y}}}$$

$$555 \quad R^2(y, \hat{y}) = r(y, \hat{y})^2$$

$$556 \quad slope(y, \hat{y}) = \frac{\Delta y}{\Delta \hat{y}}$$

$$557 \quad CCC(y, \hat{y}) = \frac{2r\sigma_y\sigma_{\hat{y}}}{\sigma_y^2 + \sigma_{\hat{y}}^2 + (\mu_x - \mu_{\hat{y}})}$$

558 where y are the ground truth fractions, \hat{y} are the prediction fractions, σ_x is the standard
559 deviation of x , $cov(y, \hat{y})$ is the covariance of y and \hat{y} , and $\mu_y, \mu_{\hat{y}}$ are the mean of the
560 predicted and ground truth fractions, respectively.

561 All metrics were calculated for all data points of a dataset, and separately for all data
562 points of a specific cell type. For the latter approach, we then averaged the resulting
563 values to recover single values. While in general the metrics calculated on all data
564 points are sufficient, good performance on cell type-level is important if one is to
565 compare fractions of a specific cell type between samples.

566 CIBERSORT (CS)

567 CS is a cell convolution algorithm based on specialized GEPs and support vector
568 regression. Cell composition estimations were obtained using the CS web application
569 (<https://cibersort.stanford.edu/>). For all deconvolutions with CS, we used the LM22
570 GEP, which was generated by the CS authors from 22 leukocyte subsets profiled on
571 the HGU133A microarray platform.

572 Because the LM22 GEP matrix contains cell types at a finer granularity than what was
573 used for this study, predicted fractions of sub-cell types were added together. For cell
574 grouping, we used the mapping of sub-cell types to broader types given by Figure 6
575 from Monaco *et al.*¹⁰. We provide a table with the exact mappings used here in the
576 supplementary material (Table S13). The deconvolution was performed using 500
577 permutations with quantile normalization disabled for all datasets but GSE65133
578 (Microarray), as is recommended for RNA-seq data. We used default settings for all
579 other CS parameters.

580 CIBERSORTx (CSx)

581 CSx is a recent variant of CS that can generate GEP matrices from scRNA-seq data
582 and use these for deconvolution. For additional deconvolution robustness, it applies
583 batch normalization to the data. All signature matrices were created by uploading the
584 labeled scRNA-seq expression matrices and using the default options. Quantile

585 normalization was disabled. For deconvolution on simulated data, no batch
586 normalization was used. For all bulk RNA-seq datasets, the S-Mode batch
587 normalization was chosen. All PBMC datasets were deconvolved using a GEP matrix
588 generated from the data6k dataset (for simulated samples from data6k, a donorA GEP
589 matrix was chosen).

590 MuSiC

591 MuSiC is a deconvolution algorithm that uses multi-subject scRNA-seq datasets as
592 GEP matrices in an attempt to include heterogeneity in the matrices to improve
593 generalization. While MuSiC tries to address similar issues of previous deconvolution
594 algorithms by using scRNA-seq data, the approach is very different. For
595 deconvolution, MuSiC applies a sophisticated GEP-based deconvolution algorithm
596 that uses weighted non-negative least squares regression with an iterative estimation
597 procedure that imposes more weight on informative genes and less weight on non-
598 informative genes.

599 The MuSiC R package contains functionality to generate the necessary GEP matrix
600 given a scRNA-seq dataset and cell type labels. To generate MuSiC deconvolution
601 predictions on PBMC datasets, we used the data8k scRNA-seq dataset as reference
602 data for MuSiC and follow the tutorial provided by the authors to perform the
603 deconvolution. For deconvolution of artificial samples generated from the data8k
604 dataset, we provided MuSiC with the data6k dataset as reference instead.

605 MuSiC was developed with a focus on multi-subject scRNA-seq datasets, in which the
606 algorithm tries to take advantage from the added heterogeneity that these datasets
607 contain, by calculating a measure of cross-subject consistency for marker genes. To
608 assess how Scaden performs on multi-subject datasets compared to MuSiC, we
609 evaluated both methods on artificial bulk RNA-seq samples from human pancreas. We

610 used the 'bulk_construct' function from MuSiC to combine the cells from all 18 subjects
611 contained in the scRNA-seq dataset from Xin et al to generate artificial bulk samples
612 for evaluation. Next, as a multi-subject reference dataset, we used the pancreas
613 scRNA-seq dataset from Segerstolpe *et al.*¹⁹, which contains single-cell expression
614 data from 10 different subjects, 4 of which with type-2 Diabetes. For Scaden, the
615 Segerstolpe scRNA-seq dataset was split by subjects, and training datasets were
616 generated for each subject, yielding in total 10,000 samples. For MuSiC, a processed
617 version of this dataset was downloaded from the resources provided by the MuSiC
618 authors⁸ and used as input reference dataset for the MuSiC deconvolution.
619 Deconvolution was then performed according to the MuSiC tutorial, and performance
620 compared according to the above-defined metrics.

621 Cell Population Mapping (CPM)

622 CPM is a deconvolution algorithm that uses single-cell expression profiles to identify
623 a so-called 'cell population map' from bulk RNA-seq data⁹. In CPM, the cell population
624 map is defined as composition of cells over a cell-state space, where a cell-state is
625 defined as a current phenotype of a single cell. Contrary to other deconvolution
626 methods, CPM tries to estimate the abundance of all cell-states and types for a given
627 bulk mixture, instead of only deconvolving the cell types. As input, CPM requires a
628 scRNA-seq dataset and a low-dimensional embedding of all cells in this dataset, which
629 represents the cell-state map. As CPM estimates abundances of both cell-states and
630 types, it can be used for cell type deconvolution by summing up all estimated fractions
631 for all cell-states of a given cell type - a method that is implemented in the scBio R
632 package, which contains the CPM method. To perform deconvolution with CPM, we
633 used the data6k PBMC scRNA-seq dataset as input reference for all PBMC samples.
634 For samples simulated from the data6k dataset, we used the data8k dataset as

635 reference. According to the CPM paper, a dimension reduction method can be used
636 to obtain the cell-state space. We therefore used UMAP, a dimension reduction
637 method widely used for scRNA-seq data, to generate the cell-state space mapping for
638 the input scRNA-seq data. Deconvolution was then performed using the CPM function
639 of the scBio package with a scRNA-seq and accompanying UMAP embedding as
640 input.

641

642 **Data Availability**

643 Only publicly available datasets were used during this study. The scRNA-seq PBMC
644 datasetse donorA, donorC, data6k and data8k were all downloaded from 10X
645 Genomics (<https://support.10xgenomics.com/single-cell-gene-expression/datasets>),
646 were they are listed as 'Frozen PBMCs (Donor A)', 'Frozen PBMCs (Donor C)', '6k
647 PBMCs from a Healthy Donor' and '8k PBMCs from a Healthy Donor', respectively.
648 The Segerstolpe et al. scRNA-seq pancreas dataset was downloaded from
649 ArrayExpress with accession code E-MTAB-5061. The scRNA-seq datasets from
650 Baron et al. (pancreas), Tasic et al., Zeisel et al., Romanov et al., Campbell et al.
651 and Chen et al. (all mouse brain) were all downloaded from [https://hemberg-](https://hemberg-lab.github.io/scRNA.seq.datasets/)
652 [lab.github.io/scRNA.seq.datasets/](https://hemberg-lab.github.io/scRNA.seq.datasets/). The ascites scRNA-seq dataset was downloaded
653 from <https://figshare.com/s/711d3fb2bd3288c8483a>. The bulk RNA-seq dataset
654 PBMC1 is accessible from ImmPort with accession code SDY67. The PBMC2
655 dataset was downloaded from GEO with accession code GSE107011. The
656 ROSMAP human brain RNA-seq dataset was downloaded from Synapse (ID:
657 syn3219045). The bulk RNA-seq data from ascites was kindly provided by Schelker
658 et al. The pancreas scRNA-seq dataset from Xin et al. was accessed from the
659 MuSiC tutorial site (<https://xuranw.github.io/MuSiC/articles/pages/data.html>).

660 Code Availability

661 The source code for Scaden is available at <https://github.com/KevinMenden/scaden>.

662 Documentation is published at <https://scaden.readthedocs.io>. Code to generate the

663 figures along with the training datasets used in this study is published at figshare:

664 <https://figshare.com/projects/Scaden/62834>.

665

666 List of abbreviations

667 RNA-seq : Next Generation RNA Sequencing

668 GEP : gene expression profile matrix

669 SVR : Support Vector Regression

670 DNN : Deep Neural Network

671 scRNA-seq : single cell RNA-seq

672 simulated tissue : training data generated by mixing proportions of scRNA-seq data

673 PBMC : peripheral blood mononuclear cells

674 CCC : concordance correlation coefficient

675 r : Pearson's correlation coefficient

676 CS : CIBERSORT

677 CSx : CIBERSORTx

678 CPM : Cell Population Mapping

679 **Author information**

680 **Affiliations**

681 **German Center for Neurodegenerative Diseases Tuebingen, Germany**

682 Kevin Menden, Anupriya Dalmia, Peter Heutink, Stefan Bonn

683 **Institute of Medical Systems Biology, University Medical Center Hamburg-**

684 **Eppendorf, Germany**

685 Mohamed Marouf, Stefan Bonn

686 **Contributions**

687 KM and SB initiated the project. KM, PH, and SB designed the study, deep learning
688 models, and analysis. KM and MM built the deep learning models. KM, MM, and AD
689 analyzed the data. KM and SB wrote and MM, AD, and PH contributed to the
690 manuscript writing.

691

692 **Competing interests**

693 The authors have no competing interests.

694 **Acknowledgements**

695 We would like to thank the people of the Genome Biology of Neurodegenerative
696 Diseases group and Institute of Medical Systems Biology for helpful discussions and
697 suggestions.

698 **Funding**

699 This study was supported in part by RiMod-FTD a EU Joint Programme -
700 Neurodegenerative Disease Research (JPND) to PH, KM and SFB 1286/Z2 and
701 BMBF Integrative Data Semantics for Neurodegenerative research (IDSN) to MM.

702 **Corresponding author**

703 Correspondence to Stefan Bonn (sbonn@uke.de) and Kevin Menden
704 (kevin.menden@dzne.de).

705

706 References

- 707 1. Hrdlickova, R., Toloue, M. & Tian, B. RNA-Seq methods for transcriptome
708 analysis. *Wiley Interdiscip. Rev. RNA* **8**, (2017).
- 709 2. Egeblad, M., Nakasone, E. S. & Werb, Z. Tumors as organs: Complex tissues
710 that interface with the entire organism. *Dev. Cell* **18**, 884–901 (2010).
- 711 3. Kuhn, A., Thu, D., Waldvogel, H. J., Faull, R. L. M. & Luthi-Carter, R.
712 Population-specific expression analysis (PSEA) reveals molecular changes in
713 diseased brain. *Nat. Methods* **8**, 945–947 (2011).
- 714 4. Avila Cobos, F., Vandesompele, J., Mestdagh, P. & De Preter, K.
715 Computational deconvolution of transcriptomics data from mixed cell
716 populations. *Bioinformatics* **34**, 1969–1979 (2018).
- 717 5. Mohammadi, S., Zuckerman, N., Goldsmith, A. & Grama, A. A Critical Survey
718 of Deconvolution Methods for Separating Cell Types in Complex Tissues.
719 *Proc. IEEE* **105**, 340–366 (2017).
- 720 6. Newman, A. M. *et al.* Robust enumeration of cell subsets from tissue
721 expression profiles. *Nat. Methods* **12**, 453–457 (2015).
- 722 7. Newman, A. M. *et al.* Determining cell type abundance and expression from
723 bulk tissues with digital cytometry. *Nat. Biotechnol.* (2019).
724 doi:10.1038/s41587-019-0114-2
- 725 8. Wang, X., Park, J., Susztak, K., Zhang, N. R. & Li, M. Bulk tissue cell type
726 deconvolution with multi-subject single-cell expression reference. *Nat.*
727 *Commun.* **10**, 380 (2019).
- 728 9. Frishberg, A. *et al.* Cell composition analysis of bulk genomics using single-cell
729 data. *Nat. Methods* **16**, (2019).
- 730 10. Monaco, G. *et al.* RNA-Seq Signatures Normalized by mRNA Abundance

- 731 Allow Absolute Deconvolution of Human Immune Cell Types. *Cell Rep.* **26**,
732 1627–1640.e7 (2019).
- 733 11. Vallania, F. *et al.* Leveraging heterogeneity across multiple datasets increases
734 cell-mixture deconvolution accuracy and reduces biological and technical
735 biases. *Nat. Commun.* **9**, (2018).
- 736 12. Venet, D., Pecasse, F., Maenhaut, C. & Bersini, H. Separation of samples into
737 their constituents using gene expression data. *Bioinformatics* **17**, 279–287
738 (2001).
- 739 13. Shapiro, E., Biezuner, T. & Linnarsson, S. Single-cell sequencing-based
740 technologies will revolutionize whole-organism science. *Nat. Rev. Genet.* **14**,
741 618–630 (2013).
- 742 14. Schaum, N. *et al.* Single-cell transcriptomics of 20 mouse organs creates a
743 Tabula Muris. *Nature* **562**, 367–372 (2018).
- 744 15. Kelley, K. W., Nakao-Inoue, H., Molofsky, A. V. & Oldham, M. C. Variation
745 among intact tissue samples reveals the core transcriptional features of human
746 CNS cell classes. *Nat. Neurosci.* **21**, 1171–1184 (2018).
- 747 16. Hicks, S. C., Townes, F. W., Teng, M. & Irizarry, R. A. Missing data and
748 technical variability in single-cell RNA-sequencing experiments. *Biostatistics*
749 **19**, 562–578 (2018).
- 750 17. Lin, L. I. A Concordance Correlation Coefficient to Evaluate Reproducibility
751 Author (s): Lawrence I-Kuei Lin Published by : International Biometric Society
752 Stable URL : <http://www.jstor.org/stable/2532051> REFERENCES Linked
753 references are available on JSTOR for thi. *Biometrics* **45**, 255–268 (1989).
- 754 18. Xin, Y. *et al.* RNA Sequencing of Single Human Islet Cells Reveals Type 2
755 Diabetes Genes. *Cell Metab.* **24**, 608–615 (2016).

- 756 19. Segerstolpe, Å. *et al.* Single-Cell Transcriptome Profiling of Human Pancreatic
757 Islets in Health and Type 2 Diabetes. *Cell Metab.* **24**, 593–607 (2016).
- 758 20. Zimmermann, M. T. *et al.* System-wide associations between DNA-
759 methylation, gene expression, and humoral immune response to influenza
760 vaccination. *PLoS One* **11**, 1–21 (2016).
- 761 21. Schelker, M. *et al.* Estimation of immune cell content in tumour tissue using
762 single-cell RNA-seq data. *Nat. Commun.* **8**, 2032 (2017).
- 763 22. Bennett, D. A. *et al.* Religious Orders Study and Rush Memory and Aging
764 Project. *J. Alzheimer's Dis.* **64**, S161–S189 (2018).
- 765 23. Braak, H. & Braak, E. Neuropathological staging of Alzheimer-related
766 changes. *Acta Neuropathol.* **82**, 239–59 (1991).
- 767 24. Yosinski, J., Clune, J., Nguyen, A., Fuchs, T. & Lipson, H. Understanding
768 Neural Networks Through Deep Visualization. (2015).
- 769 25. Athiwaratkun, B., Finzi, M., Izmailov, P. & Wilson, A. G. Improving
770 Consistency-Based Semi-Supervised Learning with Weight Averaging. *Jmlr*
771 **17**, 1–35 (2018).
- 772 26. Wolf, F. A., Angerer, P. & Theis, F. J. SCANPY: Large-scale single-cell gene
773 expression data analysis. *Genome Biol.* **19**, 1–5 (2018).
- 774 27. Satija, R., Farrell, J. A., Gennert, D., Schier, A. F. & Regev, A. Spatial
775 reconstruction of single-cell gene expression data. *Nat. Biotechnol.* **33**, 495–
776 502 (2015).
- 777 28. Zeisel, A. *et al.* Molecular Architecture of the Mouse Nervous System. *Cell*
778 **174**, 999–1014.e22 (2018).
- 779 29. Love, M. I., Soneson, C., Patro, R., Vitting-seerup, K. & Oshlack, A. Swimming
780 downstream : statistical analysis of differential transcript usage following

781 Salmon quantification. 1–50 (2019).

782

783

784 Supplementary Figures & Tables

Tissue	Name	# cells	# Subjects	Source
PBMC	data6k	5,419	1	10X Genomics
PBMC	data8k	8,381	1	10X Genomics
PBMC	donorA	2,900	1	10X Genomics
PBMC	donorC	9,519	1	10X Genomics
Mouse Brain	Tasic	1,679	1	Tasic et al., Nat. Neurosci., 2016
Mouse Brain	Zeisel	3,005	1	Zeisel et al., Science, 2015
Mouse Brain	Romanov	2,881	1	Romanov et al., Nat. Neurosci., 2018
Mouse Brain	Campbell	21,086	1	Campbell et al, Nat. Neurosci., 2017
Mouse Brain	Chen	14,437	1	Chen et al., Cell Rep., 2017
Pancreas	Segerstolpe	3,514	10	Segerstolpe et al., Cell Metab., 2016
Pancreas	Baron	8,569	4	Baron et al., Cell Syst., 2016
Ascites	Ascites	3,114	3	Schelker et al, Nat. Comm., 2018

785 **Table S1** *scRNA-seq datasets used for the generation of simulated tissues for Scaden*
786 *training.*

787

788

Tissue	# Samples	# Datasets	Size
PBMC	32,000	4	1.2 GB
Pancreas	14,000	2	0.6 GB
Mouse Brain	30,000	5	1.5 GB
Ascites	6,000	1	0.38 GB

789 **Table S2** *Number of samples, datasets, and size of the simulated training data.*

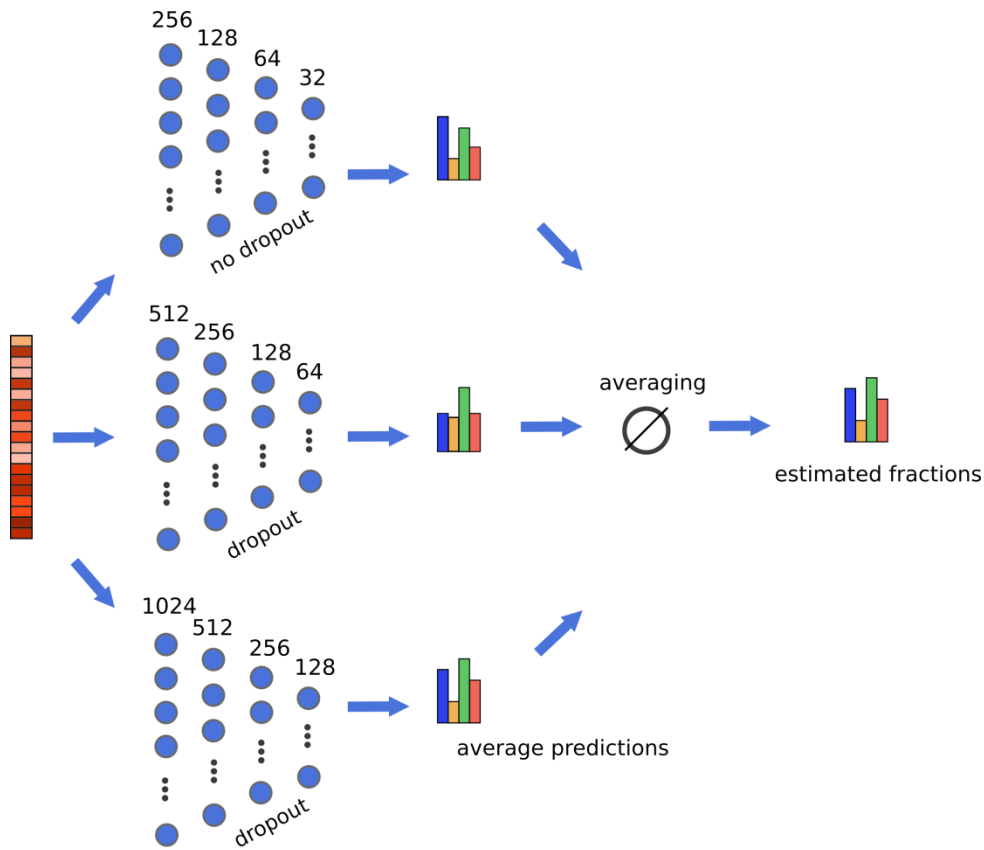
790

791

Parameter	Values tested
Batch size	32, 64, 128, 256, 512
# Layers	2, 3, 4
Layer sizes	2048, 1024, 512, 256, 128, 64, 32, 16
Dropout rate	[0, 0.8]
Loss function	L1, L2

792 **Table S3** *Hyperparameters used for model optimization.*

793



794

795 **Figure S1** Overview of the Scaden neural network ensemble model. A bulk RNA-seq
796 sample is the input to three separate deep neural networks with varying layer sizes
797 and dropout regularization. The predictions of all three models are subsequently
798 averaged to obtain the final Scaden predictions. During training, predictions are not
799 averaged and each model is trained separately.

800

Model	# Layers	Layer sizes	Dropout rates
M256	4	256, 128, 64, 32	0, 0, 0, 0
M512	4	512, 256, 128, 64	0, 0.3, 0.2., 0.1
M1024	4	1024, 512, 256, 128	0, 0.6, 0.3, 0.1

801 **Table S4** Architectures of deep neural network models used in Scaden ensemble.

802

Method	DS	RMSE	Slope	Correlation	Intercept	CCC
CPM	data6k	0.192	0.03	0.082	0.162	0.053
CPM	data8k	0.185	0.048	0.263	0.159	0.093
CPM	donorA	0.239	-0.081	-0.259	0.18	-0.147
CPM	donorC	0.189	0.038	0.102	0.16	0.066
CS	data6k	0.163	0.508	0.57	0.082	0.566
CS	data8k	0.136	0.551	0.708	0.075	0.687
CS	donorA	0.137	0.605	0.767	0.066	0.746
CS	donorC	0.168	0.45	0.522	0.092	0.517
CSx	data6k	0.106	0.756	0.824	0.041	0.821
CSx	data8k	0.097	0.744	0.863	0.043	0.854
CSx	donorA	0.125	0.696	0.81	0.051	0.801
CSx	donorC	0.094	0.829	0.865	0.029	0.864
MuSiC	data6k	0.086	0.848	0.887	0.025	0.886
MuSiC	data8k	0.136	0.663	0.728	0.056	0.725
MuSiC	donorA	0.1	0.811	0.883	0.031	0.88
MuSiC	donorC	0.084	0.897	0.896	0.017	0.896
Scaden	data6k	0.104	0.747	0.83	0.042	0.825
Scaden	data8k	0.133	0.625	0.73	0.063	0.722
Scaden	donorA	0.035	0.92	0.988	0.013	0.985
Scaden	donorC	0.046	0.849	0.973	0.025	0.964

803 **Table S5** Deconvolution evaluation on simulated PBMC data.

804

805

Method	Celltype	RMSE	Correlation	Slope	Intercept	CCC
CSx	ALPHA	0.282	0.816	0.691	0.431	0.375
CSx	BETA	0.309	0.833	0.175	-0.017	0.078
CSx	DELTA	0.04	0.812	1.567	-0.013	0.647
CSx	GAMMA	0.052	0.921	1.131	0.0	0.897
CSx	Total	0.212	0.79	1.113	-0.028	0.746
MuSiC	ALPHA	0.11	0.887	1.108	-0.042	0.863
MuSiC	BETA	0.148	0.752	1.067	0.017	0.694
MuSiC	DELTA	0.023	0.817	0.716	-0.003	0.707
MuSiC	GAMMA	0.068	0.881	0.552	-0.003	0.711
MuSiC	Total	0.099	0.938	1.078	-0.019	0.929
Scaden	ALPHA	0.067	0.949	1.071	-0.034	0.942
Scaden	BETA	0.07	0.936	1.152	-0.045	0.916
Scaden	DELTA	0.024	0.807	1.012	0.008	0.764
Scaden	GAMMA	0.045	0.914	0.89	-0.008	0.901
Scaden	Total	0.055	0.978	1.033	-0.008	0.976

806 **Table S6** Deconvolution performance on simulated pancreas data from Xin et al..

807

808

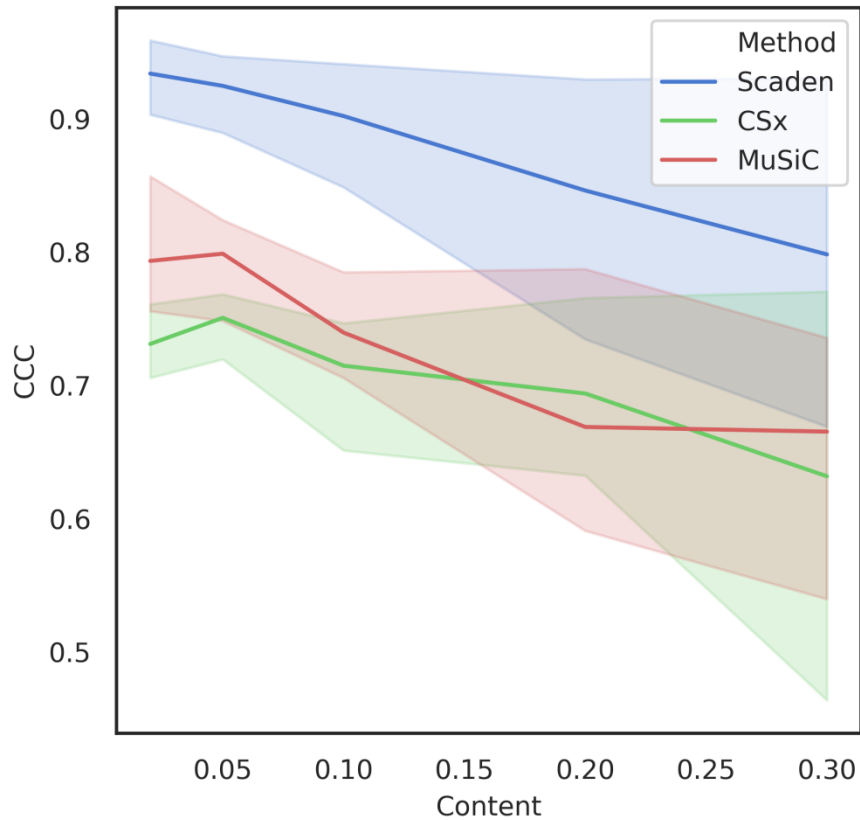
809

Tissue	Name	# Samples	Reference
PBMC	PBMC1	12	Zimmermann et al., PLOS one, 2016
PBMC	PBMC2	12	Monaco et al., Cell Reports, 2019
Pancreas	Xin	18	Xin et al., Cell Metab., 2016
Human Brain	ROSMAP	390	Bennett et al., Curr Alzheimer Res., 2012
Ascites	Ascites	3	Schelker at al., Nat. Comm. 2018

810 **Table S7** *Tissue RNA-seq datasets used for performance evaluation.*

811

812



813

814 **Figure S2** Deconvolution performance on datasets with added unknown mixture contents.

815 Unknown cell type content was added to the simulated bulk mixture in fixed concentrations

816 (5%, 10%, 20%, 30%). The deconvolution performance was assessed on samples

817 generated from the data6k, donorA and donorC datasets.

818

Method	Content	RMSE	CCC
CSx	0.02	0.097	0.731
CSx	0.05	0.092	0.751
CSx	0.1	0.092	0.715
CSx	0.2	0.091	0.694
CSx	0.3	0.099	0.632
MuSiC	0.02	0.084	0.793
MuSiC	0.05	0.083	0.799
MuSiC	0.1	0.089	0.739
MuSiC	0.2	0.095	0.669
MuSiC	0.3	0.101	0.665
Scaden	0.02	0.041	0.934
Scaden	0.05	0.044	0.925
Scaden	0.1	0.046	0.902
Scaden	0.2	0.054	0.846
Scaden	0.3	0.063	0.798

819

820 **Table S8** *Deconvolution performance on datasets with added unknown mixture*

821 *contents.*

822

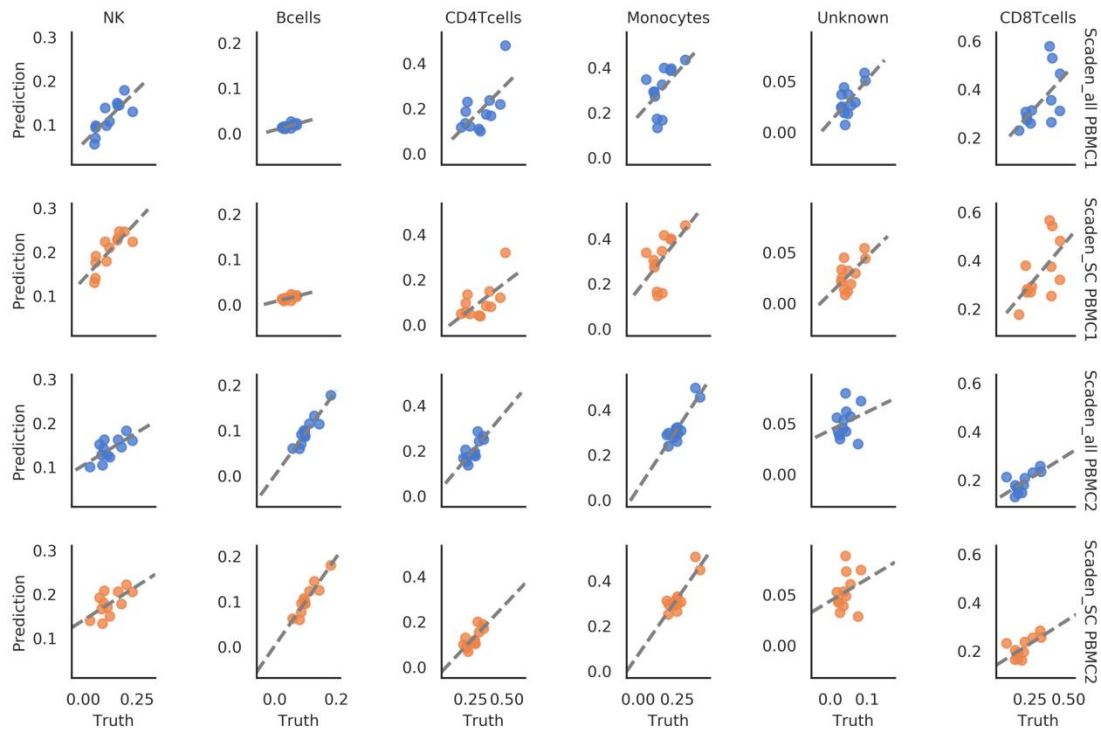
823

Method	Dataset	Celltype	RMSE	Correlation	Slope	Intercept	CCC
CPM	PBMC1	Total	0.18	-0.003	-0.003	0.167	-0.003
CPM	PBMC2	Total	0.114	-0.203	-0.094	0.182	-0.155
CS	PBMC1	Total	0.147	0.437	0.491	0.085	0.434
CS	PBMC2	Total	0.101	0.594	0.754	0.041	0.577
CSx	PBMC1	Total	0.16	0.603	0.925	0.012	0.552
CSx	PBMC2	Total	0.13	0.456	0.67	0.055	0.424
MuSiC	PBMC1	Total	0.316	-0.235	-0.468	0.245	-0.189
MuSiC	PBMC2	Total	0.299	-0.197	-0.542	0.257	-0.127
Scaden	PBMC1	Total	0.104	0.722	0.805	0.032	0.717
Scaden	PBMC2	Total	0.052	0.855	0.848	0.025	0.855

824 **Table S9** *Deconvolution performance on real PBMC RNA-seq datasets PBMC1 and*

825 *PBMC2.*

826



827

828 **Figure S3** Comparison of Scaden deconvolution results on PBMC1 and PBMC2 datasets

829 with and without (Scaden_all, Scaden_SC, respectively) bulk RNA-seq samples included in

830 training data.

831

832

Method	Dataset	Celltype	RMSE	Correlation	Slope	Intercept	CCC
Scaden_SC	PBMC1	Total	0.131	0.564	0.644	0.059	0.559
Scaden_SC	PBMC2	Total	0.077	0.684	0.689	0.052	0.684
Scaden_all	PBMC1	Total	0.104	0.722	0.805	0.032	0.717
Scaden_all	PBMC2	Total	0.052	0.855	0.848	0.025	0.855
Scaden_SC	PBMC1	Bcells	0.033	0.648	0.172	0.006	0.083
Scaden_SC	PBMC1	CD4Tcells	0.228	0.633	0.492	-0.055	0.149
Scaden_SC	PBMC1	CD8Tcells	0.101	0.603	0.761	0.108	0.562
Scaden_SC	PBMC1	Monocytes	0.178	0.556	0.885	0.173	0.186
Scaden_SC	PBMC1	NK	0.087	0.81	0.531	0.137	0.312
Scaden_SC	PBMC1	Unknown	0.029	0.577	0.361	0.009	0.287
Scaden_SC	PBMC2	Bcells	0.012	0.936	0.977	0.002	0.935
Scaden_SC	PBMC2	CD4Tcells	0.145	0.767	0.682	-0.057	0.119
Scaden_SC	PBMC2	CD8Tcells	0.049	0.67	0.403	0.129	0.587
Scaden_SC	PBMC2	Monocytes	0.078	0.865	0.994	0.071	0.558
Scaden_SC	PBMC2	NK	0.071	0.629	0.314	0.14	0.276
Scaden_SC	PBMC2	Unknown	0.025	0.247	0.217	0.044	0.209
Scaden_all	PBMC1	Bcells	0.031	0.668	0.188	0.007	0.1
Scaden_all	PBMC1	CD4Tcells	0.151	0.638	0.652	-0.017	0.345
Scaden_all	PBMC1	CD8Tcells	0.096	0.6	0.704	0.123	0.569
Scaden_all	PBMC1	Monocytes	0.172	0.518	0.777	0.184	0.177
Scaden_all	PBMC1	NK	0.036	0.804	0.488	0.058	0.71
Scaden_all	PBMC1	Unknown	0.026	0.64	0.41	0.01	0.365
Scaden_all	PBMC2	Bcells	0.013	0.936	0.94	0.0	0.917
Scaden_all	PBMC2	CD4Tcells	0.074	0.772	0.769	-0.005	0.373
Scaden_all	PBMC2	CD8Tcells	0.051	0.672	0.398	0.106	0.562
Scaden_all	PBMC2	Monocytes	0.072	0.895	1.058	0.049	0.614
Scaden_all	PBMC2	NK	0.045	0.69	0.301	0.103	0.467
Scaden_all	PBMC2	Unknown	0.023	0.241	0.178	0.043	0.203

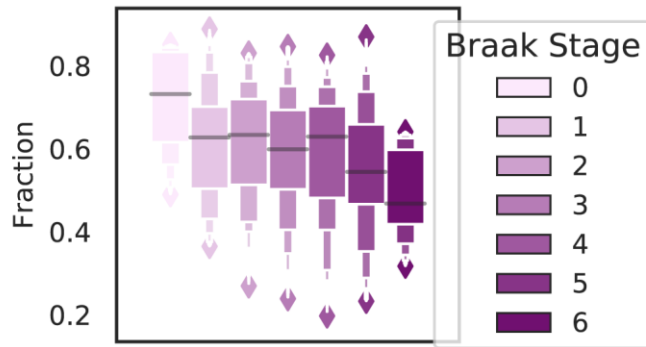
833 **Table S10** Deconvolution performance on real PBMC RNA-seq data for Scaden models
834 trained only on scRNA-seq simulated tissues (Scaden_SC) or on a mix of simulated and real
835 tissue data (Scaden_all).

836

Method	Type	CCC	Correlation	Intercept	RMSE	Slope
CPM	Total	-0.0	0.004	0.153	0.183	-0.0
CSx	Total	0.938	0.952	0.002	0.069	1.115
MuSiC	Total	0.876	0.907	0.033	0.079	0.696
Scaden	Total	0.948	0.955	-0.030	0.061	1.066

837 **Table S11** *Deconvolution performance on real Ascites RNA-seq data.*

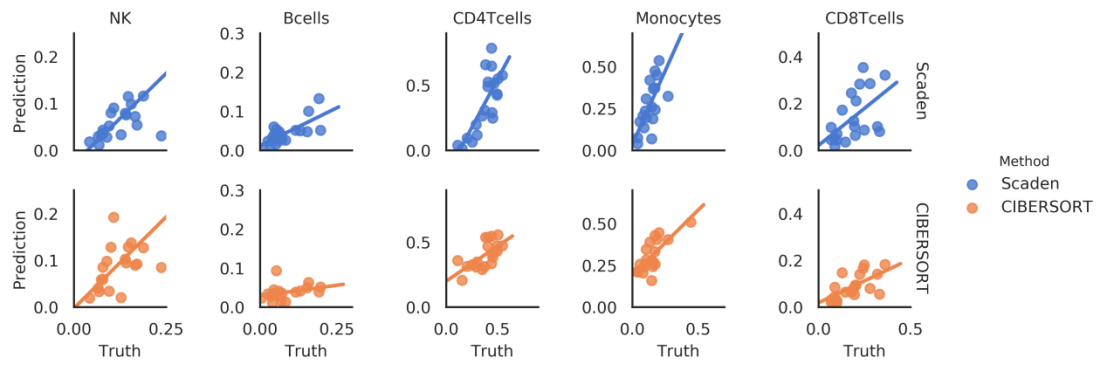
838



839

840 **Figure S4** *Deconvolution performance on real human brain RNA-seq data.* Scaden was
841 trained on mouse scRNA-seq data and the trained model was used to deconvolve cell
842 fractions of ROSMAP human brain RNA-seq data. This data does not contain cell fraction
843 ground-truth information. Instead, the box plot shows the decrease of neuronal cell fractions
844 with increasing Braak disease stage, a well-known phenomenon in AD.

845



846

847 **Figure S5** Deconvolution performance comparison of CS (LM22) and Scaden on the

848 GSE65133 PBMC microarray dataset.

849

850

Method	Celltype	CCC	Correlation	Intercept	RMSE	Slope
CS	Bcells	0.122	0.33	0.029	0.068	0.109
CS	CD4Tcells	0.629	0.658	0.199	0.095	0.537
CS	CD8Tcells	0.285	0.635	0.018	0.12	0.375
CS	Monocytes	0.295	0.741	0.19	0.17	0.779
CS	NK	0.623	0.698	-0.003	0.059	0.78
CS	Total	0.717	0.728	0.026	0.11	0.869
Scaden	Bcells	0.431	0.728	0.012	0.055	0.388
Scaden	CD4Tcells	0.64	0.778	-0.195	0.153	1.474
Scaden	CD8Tcells	0.474	0.543	0.02	0.104	0.635
Scaden	Monocytes	0.43	0.838	0.033	0.191	1.764
Scaden	NK	0.516	0.741	-0.029	0.074	0.77
Scaden	Total	0.705	0.749	-0.015	0.126	1.067

851 **Table S12** *Deconvolution performance on real PBMC microarray data.*

852

853

Software	Version
pandas	0.23.4
Python	3.6.8
Tensorflow	1.10.0
matplotlib	2.2.3
nb_conda	2.2.1
numpy	1.15.0
scipy	1.1.0
seaborn	0.9.0
anndata	0.6.9
scanpy	1.2.2
scikit-learn	0.20.0
ipython	6.5.0
python-igraph	0.7.1.post6
louvain	0.6.1
tqdm	4.7.2
igraph	0.7.1

854 **Table S13** *Software packages and versions used.*

855

856

Target Cell Type	LM22 Cell Types
B cells	B cells naive, B cells memory
CD8 T cells	T cells CD8, T cells follicular helper, T cells gamma delta
CD4 T cells	T cells CD4 naive, T cells regulatory (Tregs), T cells CD4 memory resting, T cells CD4 memory activated
NK	NK cells resting, NK cells activated
Dendritic	Dendritic cells resting, Dendritic cells activated
Monocytes	Monocytes, Macrophages M0, Macrophages M1, Macrophages M2
Unknown	Mast cells resting, Mast cells activated, Eosinophils, T cells follicular helper, T cells gamma delta, Plasma cells, Neutrophils, Dendritic

857 **Table S14** Mapping of the LM22 GEP to cell types.

858